

**Imperial College
London**

**A Comparative Study of a Physics-Informed
Neural Network and Biomechanics-Informed
Variational Autoencoder-based Generative Model
for Evaluation of Myocardial Deformation in
Cardiac MRI**

By Dhruva Tangellamudi

MRes Biomedical Research Project 2
Respiratory and Cardiovascular Research Stream
Department of Metabolism, Digestion, and Reproduction
Imperial College of London

Supervisors:
Dr. Marta Varela
Dr. Chen Qin

August 16th, 2023

Statement of Originality:

I hereby certify that this and the research to which it refers are the product of my own work, conducted during *April 2023 ~ August 2023* while enrolled in the MRes in Biomedical Research (Respiratory and Cardiovascular Stream) program at Imperial College London. Any ideas or quotations from the work of other people, published or otherwise, or from my previous work are fully acknowledged in accordance with the discipline's standard referencing practices.

Cardiac MR Images and Segmentations utilized for this study were downloaded from the Automated Cardiac Diagnosis Challenge dataset. This dataset was created from clinical exams conducted at the University Hospital of Dijon. This data was fully anonymized without any related patient-data being disclosed. This study was a comparative image registration study between the WarpPINN model designed by Lopez et al.(2022) at Pontificia Universidad Catolica de Chile and a variational autoencoder generative model designed by Qin et al.(2023) at Imperial College of London. The WarpPINN model was downloaded from the Github page of Lopez et al. The model itself was modified to be compatible with ACDC dataset.

Acknowledgements:

I would like to express my deepest gratitude to my primary supervisor, Dr. Marta Varela, for her invaluable guidance, continued encouragement, and guidance throughout the course of this study. Her expertise has been crucial in shaping the direction and quality of this study. I would also like to express my sincere appreciation for my day-to-day supervisor, Dr. Chen Qin, for her knowledge, constructive feedback, and consistent support as I navigated this project. Without their combined support, this project would not have been possible. I am very fortunate to have had the opportunity to work under their mentorship.

Abstract:

Purpose: This study focuses on comparing two biomechanics-informed machine-learning models for cardiac cine-MRI image registration: The WarpPINN model and Qin et al.'s variational autoencoder(VAE) generative model. The goal is to determine the efficacy of these approaches for precise modeling of myocardial motion and deformation calculation.

Methods: This study utilized a subset of the ACDC dataset, containing cardiac cine-MRI images with manual segmentations from 40 subjects, including 10 normal and 30 cardiomyopathy cases: dilated (n=10), hypertrophic(n=10), and infarction-associated cardiomyopathy(n=10). The WarpPINN model was trained to register images by predicting nonrigid transformations, optimizing image similarity and alignment with biomechanical partial differential equations. Accuracy was evaluated using mean square error(MSE), structural similarity index(SSIM), Dice scores, and mean contour distance(MCD).

Results: The WarpPINN model demonstrated consistent image accuracy with low MSE (mean: $0.166 \pm 0.054 \text{ px}^2$) and high SSIM (mean: 0.849 ± 0.097). MSE by pathology: NOR(mean: $0.176 \pm 0.060 \text{ px}^2$), DCM(mean: $0.152 \pm 0.042 \text{ px}^2$), HCM(mean: $0.180 \pm 0.045 \text{ px}^2$), MINF(mean: $0.156 \pm 0.068 \text{ px}^2$). SSIM by pathology: NOR(mean: 0.807 ± 0.110), DCM(mean: 0.887 ± 0.097), HCM(mean: 0.861 ± 0.080), MINF(mean: 0.839 ± 0.101). Compared to the VAE model, WarpPINN exhibited a lower dice score (0.542 vs. VAE's 0.773), but MCD values were comparable between WarpPINN (1.808 mm) and the VAE model (2.333 mm). WarpPINN showed lower incompressibility with a mean difference in the Jacobian determinant of 0.122.

Conclusion: The WarpPINN model showcased versatility in image registration across various cardiomyopathies, but fell short in achieving the same structural accuracy as a VAE generative model. This underscores the need for ongoing refinement to enhance its precision for improved diagnostics and treatment planning in cardiac pathologies.

Keywords: Physics-Informed Neural Networks, Image Registration, Myocardial Strain, Cardiac MRI, Deformation Fields, Image Warping, Medical Imaging

Table of Contents

Statement of Originality:	2
Acknowledgements:	2
Abstract:	3
1.1: Cardiovascular Disease	5
1.2: Metrics for Heart Failure Diagnosis	5
1.3: Image Registration in Cardiovascular Magnetic Resonance Imaging	6
1.4 Cardiac Cine-Magnetic Resonance Imaging	7
1.5: Physics-Informed Neural Networks	7
1.5: WarpPINN	8
1.6: Training WarpPINN	10
1.7: 3D Deformation Modeling	10
1.7: Comparative Performance	11
1.8: Variational-Autoencoder Generative Model	12
1.9: Automatic Cardiac Diagnosis Challenge Dataset	14
1.10: Hypothesis and Aims	14
Materials and Methods:	15
2.1: Image Selection	15
2.2: Data Preprocessing	16
2.3: Mesh Generation	16
2.4: WarpPINN Architecture	18
2.5: Similarity Metrics	19
Mean Square Error	19
Structural Similarity Index Measure	19
Sorensen-Dice Coefficient	19
Mean Contour Distance	20
Results	21
3.1: 3D Mesh Results	21
3.2: Independent Performance of WarpPINN Model on ACDC Dataset	21
3.3: Performance of WarpPINN vs VAE Generative Model on ACDC Dataset	23
Discussion	25
4.1: Comparative Analysis of Biomechanical Models	25
4.2: Limitations	26
Model Assumptions	26
Mesh Generation	27
Discrepancy in Myocardial Incompressibility	27
4.3: Future Studies	28
Conclusion	29
References	29
Appendix A: Abbreviations	31
Appendix B: Pathology Descriptions Included in ACDC Dataset	32

Introduction:

1.1: Cardiovascular Disease

Cardiovascular disease(CVD) is the leading cause of global mortality and has disabled millions of people across the world. Over the past two decades, the prevalence of CVD has almost doubled from 271 million in 1991 to 523 million in 2019 with mortality rates rising by 50% during that timespan [1]. Disability-adjusted years (DALYs) have also doubled 17.7 to 34 million over the past 20 years. CVD does not just affect life expectancy but also leads to severe physical and social debilitation as well as psychological distress leading to a significantly lower quality of life [1, 2]. Given its significant impact, it is imperative that we find more reliable and efficient metrics to diagnose cardiovascular disease to facilitate prompt therapy.

1.2: Metrics for Heart Failure Diagnosis

For decades, left ventricular ejection fraction(LVEF) has been the most commonly utilized clinical imaging metric to evaluate and quantify the mechanical performance of the heart [3]. However, in recent years, myocardial strain has been found to be a viable alternative to LVEF as an advanced measure of cardiac function due to its greater sensitivity to subtle changes in cardiac inotropy and easy reproducibility [4, 5]. Specifically, myocardial strain is a measure of the change in myocardial fiber length after stress is applied. It is a dimensionless index of total ventricular deformation through the cardiac cycle (often expressed as a percentage). Myocardial fibers change in orientation based on their location in the myocardium allowing the myocardium to deform in multiple directions. Therefore, myocardial strain can be categorized based on its orientation: circumferential, longitudinal, or radial as illustrated in Figure 1.1 [4, 6].

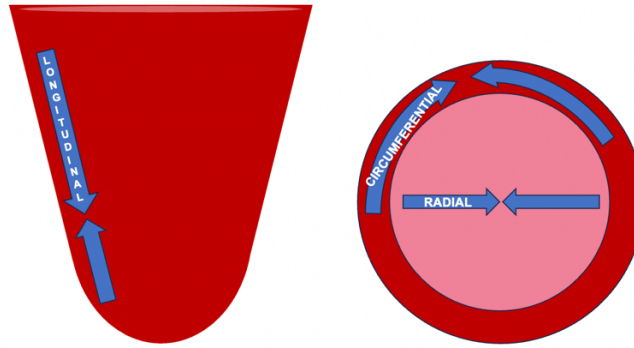


Figure 1.1: Illustration of Myocardial Strain Orientations(Longitudinal, Radial, Circumferential): Left – Long-axis view of myocardium depicting longitudinal strain(deformation of myocardial fibers along the longitudinal axis of the heart from apex to base). Right – Short-axis view of myocardium depicting radial strain(perpendicular deformation of myocardium in relation to its center) and circumferential strain(deformation of the myocardium along its perimeter or circumference).

Although traditionally LVEF has been the standard for detecting heart failure, strain has found to be a more sensitive biomarker as 40% of heart failure patients have a normal ejection fraction(LVEF > 50%) [5]. As a result of its greater sensitivity, ventricular dysfunction can be detected earlier with myocardial strain than ejection fraction. Moreover, myocardial strain can assist in detecting additional pathologies with frequently normal LVEF such as myocarditis or ischemia, and has proven to be a versatile and effective tool for diagnosing other cardiac conditions: valvulopathies, arrhythmias, dyssynchrony, and cardiomyopathies [5].

1.3: Image Registration in Cardiovascular Magnetic Resonance Imaging

In order to derive myocardial strain from cardiac imaging, the motion of the ventricular walls is characterized with a deformation field: a vector field representing how the points in one frame of an image shift and align with the corresponding points in another frame. By quantifying deformation vectors of the image points, the strain of the myocardium can be extrapolated by calculating the length of a particular deformed segment in a given direction and comparing the change in its length to its original length expressed as a percentage [7]. In order to generate the deformation field, it is necessary to first identify the points contained within the region of the

myocardium across various time frames during systole and diastole. Registering these image frames facilitates constructing an accurate rendering of the myocardium's motion over time.

1.4 Cardiac Cine-Magnetic Resonance Imaging

In this study, we utilize cardiac cine-MRI imaging for registration as it is the gold standard for assessment of global and regional wall motion visualization and overall left ventricular systolic function and is clinically widely available. This imaging modality provides an assessment of biventricular function, and volumes while also providing visualization of signs of myocardial tissue injury such as perfusion, edema, and fibrosis as a result of myocarditis or ischemia [8, 9].

1.5: Physics-Informed Neural Networks

Over the last two decades, myocardial strain analysis using Cine-MRI and echocardiography images has been extensively researched. Numerous machine-learning models have been developed for cardiac image registration, aiming to improve accuracy in deformation fields and myocardial strain values. This study focuses on a novel approach to cardiac image registration by employing physics-informed neural networks (PINNs). In 2008, physics-informed neural networks (PINNs) debuted as a novel machine learning approach, finding widespread use in natural sciences for precise modeling of real-world mechanics based on physics-derived partial differential equations [10].

PINNs are designed to derive a function, $u(x)$, a solution for the partial differential equations for the system of interest that is consistent with the available experimental data. This method is particularly useful when data is sparse or incomplete, but the system can be physically modeled. The neural network will approximate this function by minimizing a loss function, $L(\theta)$, that is a function of the data, the boundary conditions, and the differential equations describing

the physics of the system where θ is the NN parameterization [11]. A generalized form of this function is depicted in Equation 1[11]. Component A is the mean square difference(MSE) between the neural network's predicted data, $u(x_i^d; \theta)$, and the reference data, \hat{u}_i , for points x_i^d contained within our domain Ω . If $\mathcal{N}[u]$ represents a differential operator acting on the function u , component B represents the MSE of the PDE conditions, penalizing the network when it does not satisfy $\mathcal{N}[u] = 0$ for a set of a randomly selected collocation points, x_k^c .

$$L(\theta) = \overbrace{\frac{1}{N_d} \sum_i^{N_d} (u(x_i^d; \theta) - \hat{u}_i)^2}^{\text{A}} + \overbrace{\frac{1}{N_c} \sum_k^{N_c} (\mathcal{N}[u](x_k^c; \theta))^2}^{\text{B}} \quad (1)$$

1.5: WarpPINN

The focus of our study will be WarpPINN, an innovative PINNs-based method of cine-MRI left ventricular image registration and strain calculation [11]. As mentioned above, calculating myocardial strain relies on finding a suitable deformation mapping, φ , to model the motion of the myocardium over time t such that when φ is applied to an initial image of the myocardium, the result aligns with a target image at time t . For the sake of this study, the initial image will be denoted as the reference image R and the later image will be the template image T . In the WarpPINN model, R is the image of the end-diastolic left ventricle at time t_0 , while the template image is any other proceeding frame of the image T_N at time t_N . These frames will be input to the model which will predict a nonrigid transformation (φ) between R and T_N .

The predicted deformation field $\varphi(X; \theta)$ is function of the input points X of our reference image and the function $u(X; \theta)$ learned and output by the FCNN. The myocardium and the background are to modeled as hyperelastic solids. Hyperelastic solids remain elastic even when subject to exceedingly large strain values and are near incompressible. These properties allow them to be used as models of soft tissue such as the myocardium that are biomechanically similar [12].

WarpPINN's loss function integrates hyperelastic regularisation terms for the myocardium

($W(\varphi(X_j^{LV}; \theta))$) and the background ($W(\varphi(X_k^{bg}; \theta))$) and is defined as follows [11]:

$$L(\theta) = \frac{1}{N_d} \sum_i^{N_d} (R(X_i^d) - T(\varphi(X; \theta)))^p + \mu \left(\frac{1}{N_{LV}} \sum_j^{N_{LV}} W(\varphi(X_j^{LV}; \theta); \lambda_{LV}) + \frac{1}{N_{bg}} \sum_k^{N_{bg}} W(\varphi(X_k^{bg}; \theta); \lambda_{bg}) \right) \quad (2)$$

Similarity Metric
Hyperelastic Regularisation for Myocardium
Hyperelastic Regularisation for Background

The myocardium is constrained with a Neo-Hookean hyperelastic strain energy function W acting as a regulariser for the predicted displacement as shown below[11]:

$$W(\varphi; \lambda) = \text{Tr}(C) - 3 - 2 \log(J) + \lambda(J - 1)^2 \quad (3)$$

with C being the first invariant of Cauchy-Green deformation tensor ($C = F^T F$ where $F = d\varphi/dX$) and J is the Jacobian determinant of the deformation gradient ($J = \det(F)$) [11].

The loss function penalizes the difference between R and a predicted reference image $T(\varphi(X; \theta))$ reconstructed by applying deformation mapping, φ , to the template image T corresponding to component A in Equation 1. Similarly, hyperelastic regularisation corresponds to component B. When a material is incompressible, its volume is conserved despite deformation. Therefore, as the Jacobian reflects changes in an element's volume, when $J = 1$ there are no discernible changes in volume and is incompressible. Consequently, strain function penalizes changes in volume with the $(J - 1)^2$ as this term will be 0 when the incompressibility constraint is satisfied. The λ parameter regulates how strongly this incompressibility is enforced in the myocardium as well as the background [11].

1.6: Training WarpPINN

WarpPINN estimates a deformation field u for the 3D image such that for a given point p with coordinates (X, Y, Z) , $(X, Y, Z) + u(X, Y, Z, t; \theta)$ will be p 's new location at a time t . As mentioned above, the reference image, R , is the first frame of the image at $t = 0$. In the ACDC dataset, this frame is also the image of the myocardium at end-diastole or its most relaxed state with maximum blood volume. The remainder of the subsequent frames are utilized as template images T contained within the time interval $[0, 1]$, equispaced, with the last(N -th) frame corresponding to $t = 1$. The neural network trains to learn the deformation field from R to each j -th frame of the template image T_j . To evaluate the accuracy of the predicted deformation, the following loss function is derived using the similarity metric between the reference image and the template image warped by the deformation field for a normed space with $p = 1$. This similarity metric can be visualized in Equation 1. The neo-Hookean regularisation term is evaluated by sampling the points in the myocardium and background regions. Finally, the reference image is reconstructed with the predicted deformation field with trilinear interpolation. For the sake of computational efficiency, rather than evaluating the loss for every frame, the loss is computed for a single randomly chosen template frame T_j per iteration. The loss computed at time t_j is fed back to the model and the weights are adjusted accordingly [11].

1.7: 3D Deformation Modeling

When modeling deformation of the myocardium during training, WarpPINN utilizes a surface and volumetric mesh of the left ventricle across systole and diastole. A mesh is a collection of vertices, edges, and faces that define the shape and surface geometry of a three-dimensional object such as the left ventricle. It allows the model to represent a complex three-dimensional surface in a discrete and computationally efficient manner. When a subgroup of points or a portion of the mesh is displaced during each iteration, it leads to a biomechanically plausible

change in the location and intensity of other points in the image through trilinear interpolation based on the biomechanical constraints placed on the model [13]. For this study, meshes are generated utilizing Delaunay triangulation. This is the most common method of tetrahedral mesh generation without overlap or void space. This technique retrieves sample points by forming circles in which each circle contains 3 sample points on its circumference, but with no other points in that circle's domain. The points are then connected to form a triangular cell. This triangulation maximizes the minimum angle formed within a cell through edge-flipping [14].

1.7: Comparative Performance

WarpPINN's performance was compared to multiple notable models for cardiac image registration including: Temporal Diffeomorphic Free Form Deformation(TDFFD), iLogDemons, and CarMEN. The TDFFD model replicates the deformation employing B-splines, mathematical constructs used to interpolate the points of the myocardium with a smooth curve or surface that is defined by a basis function. The TDFFD utilizes B-splines to model the velocity of the myocardium and integrates the velocity field to form a deformation field while maintaining temporal consistency [15, 16]. Alternatively, the iLogDemons model is based on non-linear registration method utilizing image intensity gradients to register corresponding structures in the myocardium across time frames. This model also constructs a velocity field to derive the deformation of the myocardium while imposing soft-tissue elasticity and incompressibility to improve myocardial strain estimation [17, 18]. Finally, the CarMEN model harnessed deep learning with a convolutional neural network (CNN) to autonomously learn the motion of the myocardium and generate a deformation field that accurately aligns the images. However this model did not incorporate biomechanics and instead uses a Jacobian regularisation to ensure smoothness of the deformations[19].

Despite the considerable efficacies of these various methods, Lopez et al. demonstrated superior accuracy of PINNs through the WarpPINN model in comparison to the techniques mentioned above. By utilizing a publicly available dataset through the Cardiac Atlas Project and examining the error between landmarks in the reference and predicted images, the median of the WarpPINN error was noted to be 3.13 mm. This was lower than the median error values of 3.17 mm, 4.87 mm, and 3.8 mm of the CarMEN, TDDFD, and iLogDemons registration models respectively when applied to same dataset[11].

1.8: Variational-Autoencoder Generative Model

However, it is unclear how WarpPINN may perform in comparison to a 2020 innovation in image registration utilizing a generative model coupled with a variational autoencoder (VAE) proposed by Qin et al. as both models utilize regularisation based on cardiac biomechanics [20]. This generative VAE model trains a temporal VAE to learn the deformations of the left ventricle constrained by biomechanical principles. A VAE is a type of machine learning generative model that consists of an encoder that transforms input data into a probabilistic distribution in a lower-dimensional latent space. The decoder then samples from this latent distribution and reconstructs the original data. During training, VAEs aim to optimize their parameters to minimize the reconstruction error while also encouraging the learned latent space to adhere to a predefined distribution. The temporal VAE designed by Qin et al. uses this same framework but utilizes 2D sequential imaging data that the encoder maps into a Gaussian latent space and the decoder then generates sequences of biomechanically plausible deformations.

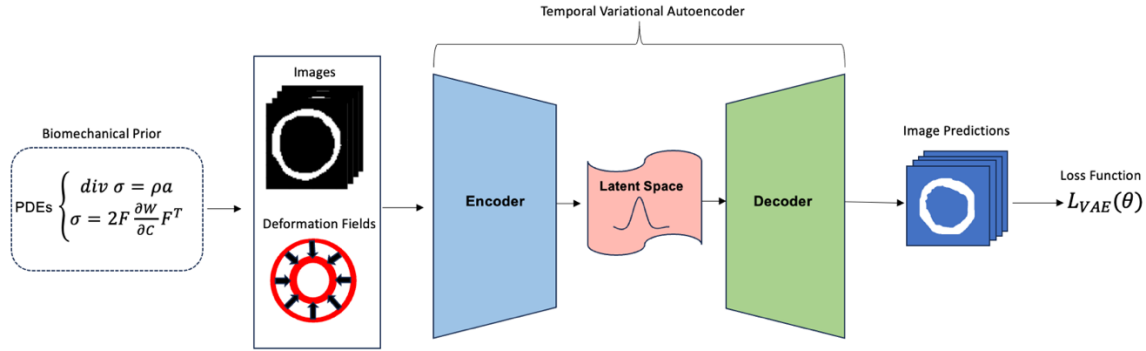


Figure 1.2: Temporal VAE Model Architecture: The biomechanical prior informs the latent space of plausible biomechanical deformations. The encoder maps sequential images into the latent space which is a lower dimensional probabilistic representation of the data in a Gaussian distribution. The decoder then samples the latent space and generates plausible deformations and generates images that align with these fields. The images are then evaluated by the loss function $L_{VAE}(\theta)$ with weight θ .

Qin et al.'s VAE generative model differed from other contemporary models by incorporating biomechanical regularisation through machine learning rather than being explicitly parameterized. By doing so, the VAE regulariser could be integrated with any registration neural network to find solutions that are biomechanically plausible. This model was tested on 2D cine-MRI images in the Automated Cardiac Diagnosis Challenge(ACDC) dataset showing exceptional image registration with mean Dice scores of approximately 80% as well as low mean contour distance with similar if not improved incompressibility of the ventricular myocardium [20].

The VAE generative model not only demonstrated better performance in image registration compared to other contemporary models, but was also shown to have better generalizability than conventional L2 regularisation methods when tested on pathologic imaging including cardiomyopathy, infarction, cardiac hypertrophy, and right ventricular dysfunction. The WarpPINN model, on the other hand, has only been validated on MRI images with normal left ventricular function [20].

1.9: Automatic Cardiac Diagnosis Challenge Dataset

This study introduces a novel dataset known as the Automated Cardiac Diagnosis Challenge (ACDC) dataset [21]. The dataset comprises 150 cardiac cine MRI divided into five subgroups: 30 normal subjects (NOR), 30 patients with myocardial infarction (MINF), 30 with dilated cardiomyopathy (DCM), 30 with hypertrophic cardiomyopathy (HCM), and 30 with abnormal right ventricle (RV). Details of these pathologies can be found in Appendix B. Each patient's exam includes weight, height, diastolic and systolic phase instants, as well as ground truth myocardial segment labels [21]. The images were collected over a six-year period using 1.5 T and 3.0 T MRI scanners, with each slice obtained in a different breath-hold using a steady-state free precession (SSFP) sequence. The dataset encompasses short-axis slices covering the left ventricle (LV) from base to apex, with slice thickness varying between 5 mm and 8 mm. The in-plane resolution ranges from 1.37 to 1.68 mm²/pixel, and the temporal sequences consist of 28 to 40 frames per cardiac cycle. The dimensions of the images are approximately 200 by 250 pixels by 10 slices in the x, y, and z directions, respectively, with an average of 11 timeframes from end-diastolic to end-systolic phases. This dataset was compiled based on clinical exams conducted at the University Hospital of Dijon and classified according to corresponding medical reports [21].

1.10: Hypothesis and Aims

The WarpPINN model and the VAE generative model are both informed by biomechanics. However, the VAE model utilizes a biomechanical prior and was designed for 2D imaging while the WarpPINN model integrates biomechanical partial differential equations in the training of a neural network and was designed to also incorporate 3D imaging.

As both models are biomechanics-informed but utilize different methodologies, we propose a comparative study of the WarpPINN model and the biomechanics-informed VAE generative

model utilizing the ACDC imaging dataset. This study will also assess the generalizability of the WarpPINN model by applying it to different cardiomyopathies included in the ACDC dataset.

Hypothesis: As both models incorporate biomechanics of the myocardium, the WarpPINN model will have similar accuracy of cardiac cine-MRI image registration to that of the VAE-generative model designed by Qin et al.

Aims:

1. Quantify and characterize the accuracy of the WarpPINN model for cardiac image registration on the ACDC dataset.
2. Investigate the generalizability of WarpPINN model by comparing image registration performance across three pathologies: dilated cardiomyopathy, hypertrophic cardiomyopathy, and myocardial infarction with altered left ventricular ejection fraction, as well as normal function.
3. Assess whether the WarpPINN model and the VAE-generative model exhibit comparable registration accuracy on the ACDC dataset.

Materials and Methods:

2.1: Image Selection

As we are comparing the WarpPINN model to the VAE generative model, we utilized the same subset of images from the ACDC dataset that Qin et al. used in their testing set. Our testing set used CMRI images from 10 subjects from the normal subset and 10 from each of the cardiomyopathy subsets(DCM, HCM, MINF) with total testing size of 40 patient images.

2.2: Data Preprocessing

In order to improve efficiency and expedite training of the PINN model, the images are cropped to isolate the left ventricle and reduce image size prior to input. In order to facilitate processing multiple images, we constructed an automated cropping method. The method encloses the region of interest (ROI) in a bounding box in each 2D slice by labeling the connected regions of the mask. The coordinates of the bounding boxes are compared to find a unified bounding box with the minimum dimensions required to encapsulate the entire ROI with a 5-pixel buffer. The coordinates of the unified box are then used to crop the image to capture the left ventricle myocardium in every slice (Figure 2.1).

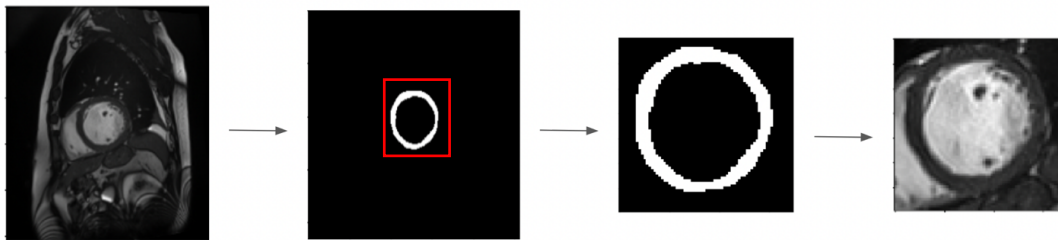


Figure 2.1: Automated Cropping: The left ventricle myocardium segmentation is cropped via labeling and creating a bounding box (red) enclosing the segmentation. The coordinates of the bounding box are then applied to crop the image.

2.3: Mesh Generation

WarpPINN utilizes a surface (Figure 2.3A) and volumetric mesh (Figure 2.3B) for modeling the deformation of the left ventricle across systole and diastole. An automated surface and volumetric mesh construction method was designed for input into the WarpPINN model utilizing Python's Scikit-Image library from the aforementioned binary mask of the myocardium. The surface mesh of the myocardium is created with triangular cells utilizing the marching cubes algorithm. The isosurface value at which the surface is extracted was set to 1×10^{-12} with descending gradient evaluation and spacing according to the pixel dimensions of the image.

The Lewiner method was chosen for surface reconstruction without degenerate triangles. The resultant generated mesh is formatted as an unstructured grid.

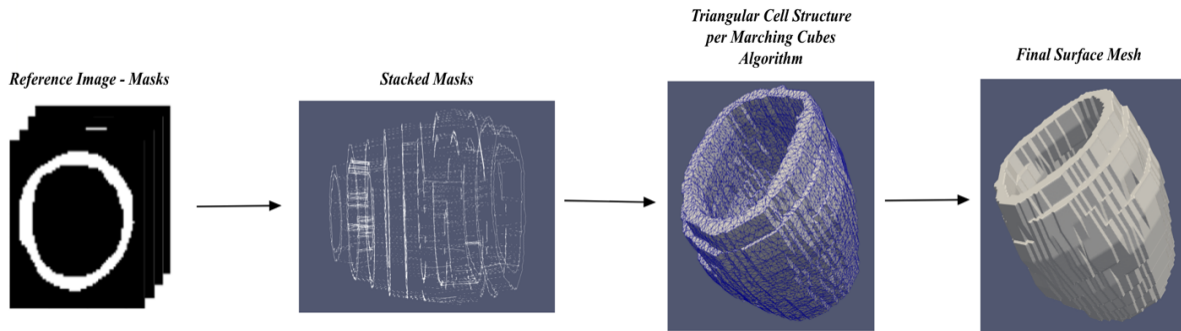


Figure 2.2: Surface mesh of left ventricle is constructed from stacked myocardial binary masks utilizing the marching cubes algorithm with Python's Scikit-Image library to create an unstructured grid with a triangular cell structure.

The volumetric mesh is then constructed as a tetrahedral unstructured grid by partitioning the 3D domain of the surface mesh using python's TetGen library. This method fits domains with arbitrarily complex geometries and can easily be refined as well as automated. TetGen is a mesh generator that takes the surface mesh's triangular cell structure and point coordinates as inputs to create a volume mesh through Delaunay triangulation [22]. To ensure a higher quality mesh, we specified a minimum dihedral angle of 25 degrees with a minimum ratio of the tetrahedral circumradii to their smallest edge length of 1.1. This method mesh generation method has been shown to be robust and effective specifically in cardiac chamber reconstruction as described by Wan et al in 2013 [23].

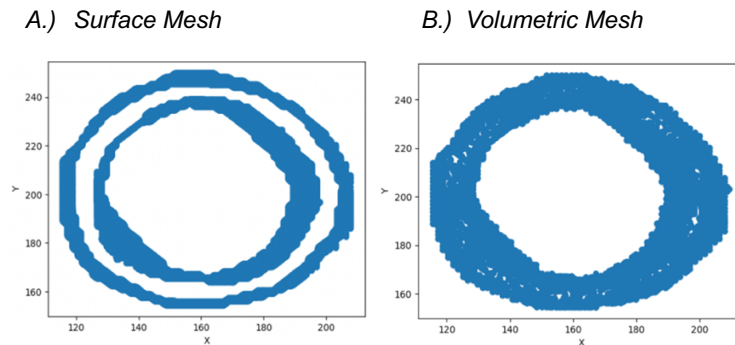


Figure 2.3: The cross sections of our surface(A) and volumetric(B) meshes are displayed above. While the surface mesh represents only the outer boundary of the object, the volumetric mesh illustrates the object's entire composition with a grid-like structure, in this case, composed of tetrahedral cells.

2.4: WarpPINN Architecture

The WarpPINN model is fully connected neural network constructed with the TensorFlow library and consists of the input layer, five hidden layers, and the output layer. The input layer contains four nodes, for the x, y, z coordinates and the time t . By default, each hidden layer contains 64 nodes and the output consists of 3 nodes containing the x, y, z displacements of the deformation field from the reference image to the template image. The network is trained using an Adam optimizer for 10,000 iterations with a batch size of 1000 [11]. Training time approximately 40 minutes [11].

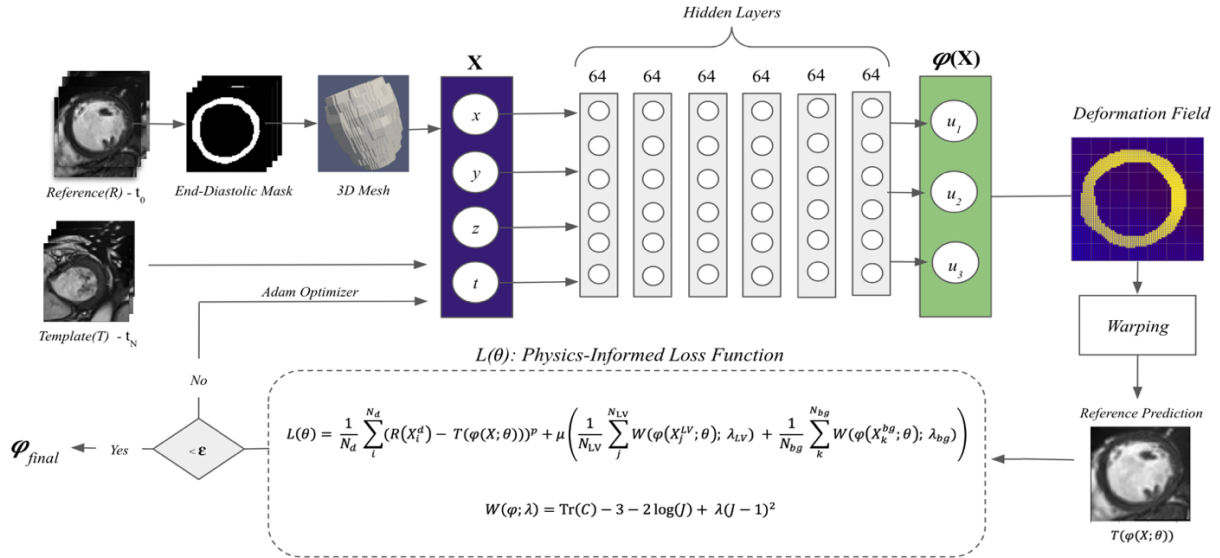


Figure 2.4: WarpPINN Architecture – WarpPINN takes as input a reference image(R) at end-diastole(t_0), from which a 3D surface and volume mesh is created, as well as the N -th frame of template image(T) at time t_N . The input layer consists of x, y, z coordinates of these images as well as the time frame. The network with then predicts a deformation field(φ) with x, y , and z components(u_1, u_2, u_3). A predicted reference image($T(\varphi(X; \theta))$) is constructed from warping T with the deformation field. The physics-informed loss is computed and if the error is greater than our preset error threshold(ϵ), the Adam optimizer adjusts the deformation field accordingly until the deformation is finalized(φ_{final}) from which the myocardial strain can be computed.

2.5: Similarity Metrics

The accuracy of the deformation field is evaluated by the similarity between the original reference image and the predicted reference image constructed by applying the deformation field to the template image. We will use the following metrics to assess registration accuracy:

Mean Square Error

Mean Square Error (MSE) is a commonly used metric to quantify the average squared difference between the reference and the predicted images within a dataset [24]. For the i -th pixels r and t in the j -th slice of the reference image R and template image T respectively, with N total pixels per image, the mean square error is calculated as follows:

$$MSE(R_j, T_j) = \frac{1}{N} \sum_i (t_{j,i} - r_{j,i})^2$$

Structural Similarity Index Measure

The SSIM is computed utilizing the mean pixel values of $R(\mu_{R_j})$ and $T(\mu_{T_j})$ as well as their respective variances $\sigma_{R_j}^2$ and $\sigma_{T_j}^2$ and the cross-variance between the two images($\sigma_{R_j T_j}$):

$$SSIM(R_j, T_j) = \frac{2\mu_{R_j}\mu_{T_j} + c_1}{\mu_{R_j}^2 + \mu_{T_j}^2 + c_1} \frac{2\sigma_{R_j T_j} + c_2}{\sigma_{R_j}^2 + \sigma_{T_j}^2 + c_2}$$

Where c_1 and c_2 are constants used for numerical stability and to avoid division by zero. The default values are used for c_1 and c_2 where $c_1 = (k_1 L)^2$ and $c_2 = (k_2 L)^2$ with $k_1 = 0.01$, $k_2 = 0.03$, and L is the maximum possible pixel value of 65535 [25].

Sorensen-Dice Coefficient

Per patient, the ACDC dataset contains a segmentation of the end-diastolic reference image(R_{seg}) as well as a segmentation of the end-systolic frame of the image. However, in order

to compare the segmentations, we must first construct a segmentation of the predicted image. This is done by applying the deformation field predicted by the neural network to the segmentation of our reference image through trilinear interpolation in order to create a warped segmentation image. This will act as the segmentation of our image prediction(P_{seg}). The Sorensen-Dice similarity coefficient or Dice score measures the spatial overlap of these segmentations and can be calculated as below [25]:

$$Dice = \frac{2 * |R_{seg} \cap P_{seg}|}{R_{seg} + P_{seg}}$$

Mean Contour Distance

As an additional validation metrics, we also compute the mean contour distance (MCD) between the contours of our reference and predicted end-systolic image segmentations. Using the Python's OpenCV package, the contours of each slice of both segmentations are delineated and their respective points are grouped. A distance matrix M representing the Euclidean distances(d_i) between each point, p_{ref} , in the reference segmentation contour and each point, p_{pred} , in the predicted segmentation contour. M is then used to calculate the mean contour distance. The MCD is defined as the average minimum distance between each point in the reference contour and its most proximal point in the predicted contour. MCD is computed for every slice of the end-systolic segmentations are compiled and the mean of these values are returned respectively.

$$MCD = \frac{1}{N} \sum_i^N d_i$$

All metrics will be reported as mean +- std unless otherwise stated. All statistical tests are conducted at a significance level of 0.05.

Results

3.1: 3D Mesh Results

Of the 40 cine-MRI images in our testing dataset, our automated mesh generation method was only able to construct a triangular surface mesh and tetrahedral volumetric mesh for 38 of these images. The two cine-MRI images that were unable to be successfully converted to a volume mesh (patient014 and patient019) were both part of the DCM subset in which the myocardium walls are generally thinner and less robust. The TetGen package was unable to tetrahedralize the points in these thinner complex structures with Delaunay tetrahedralization.

3.2: Independent Performance of WarpPINN Model on ACDC Dataset

As illustrated in Figure 3.1, the WarpPINN showed consistently low MSE ($0.166 \pm 0.054 \text{ px}^2$) and high SSIM (0.849 ± 0.097) across all 38 images tested from the ACDC dataset. In addition, this trend held true across both normal ventricular structural and the three pathological imaging sets with mean MSE values reliably less than 0.2 px^2 and SSIM values above 0.8 across the normal, DCM, HCM and MINF subsets. This evidence strongly indicated that the model can register and calculate strain for cardiac images across various disease states. Figure 3.2 provides visual examples of reference image reconstruction based on the WarpPINN model's predictions as well as highlighting imaging differences between the reference and predicted imaging. While visually similar, it is apparent from Figure 3.2 that the predicted images show some discrepancies with the reference images and loss of detail.

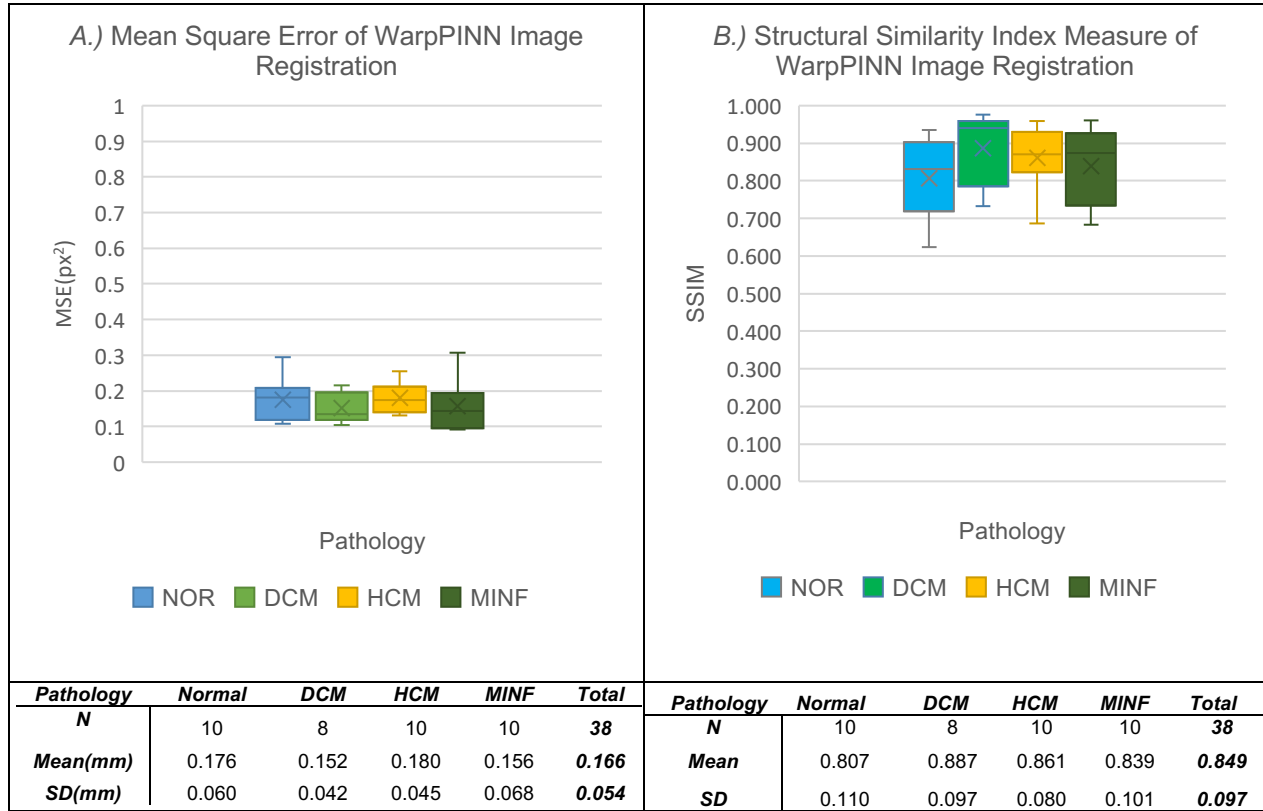


Figure 3.1: The box plots above display the distribution of Mean Squared Error(Side A - Left) and Structural Similarity Indices(Side B - Right) for the WarpPINN model's image registration of cine-MRI for pathologies in the ACDC dataset: NOR (Blue), DCM(Green), HCM (Yellow), and MINF (Brown). Each box represents the interquartile range (IQR) with the median indicated by a horizontal line inside the box. The whiskers extend to the minimum and maximum data points within 1.5 times the IQR. Lower MSE values(mean – 0.166 px²; standard deviation: 0.054 px²) and higher SSIM(mean-0.849; standard deviation: 0.097) values indicate better model performance.

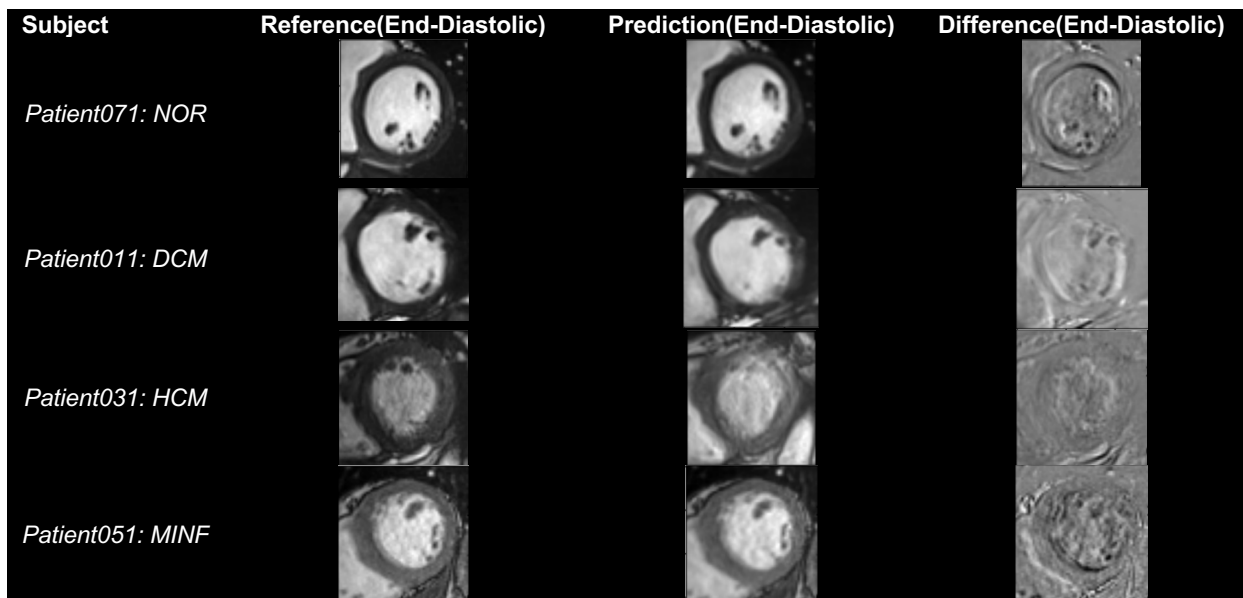
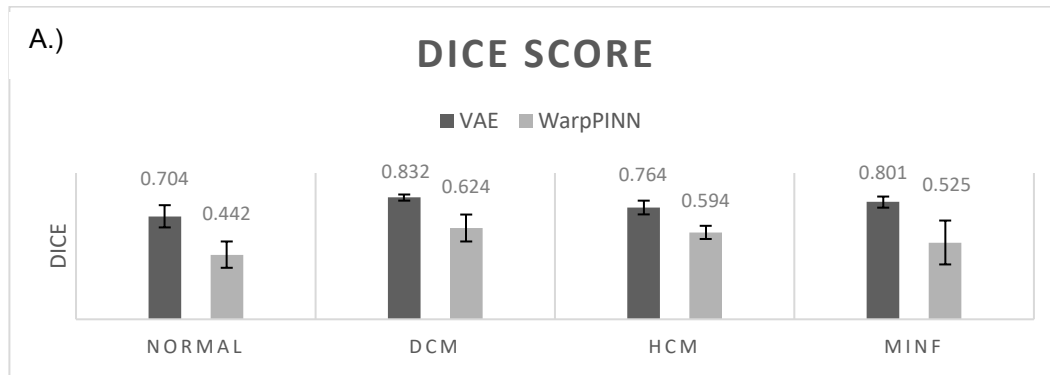


Figure 3.2: Examples of reference image reconstruction by the WarpPINN Model: The chart contains an example from images from one patient in each of our pathology subsets(NOR, DCM, HCM, MINF). The reference column contains a short-axis view of slice 3 of the of the end-diastolic left ventricle. The prediction column contains a reconstruction of that image predicted by the WarpPINN model. The difference column highlights discrepancies in these images by taking the difference between the pixel value matrices of the reference and prediction images.

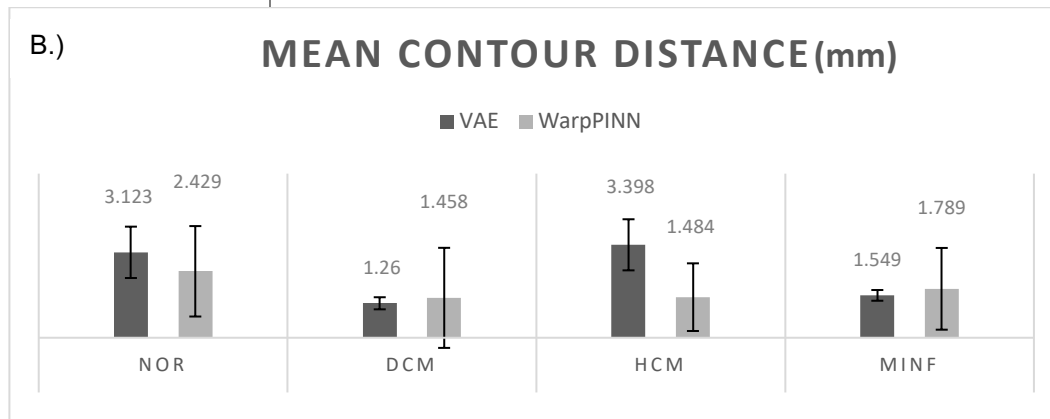
3.3: Performance of WarpPINN vs VAE Generative Model on ACDC Dataset

The WarpPINN model showed an average total dice score of 0.546 ± 0.097 indicating slightly higher than a 50% overlap of the predicted and ground truth segmentations (Figure 3.3A). This is considerably lower than the mean dice of the 0.773 ± 0.046 of the VAE model. A p-value of 0.001 indicated that the difference in dice scores was statistically significant and demonstrated that the VAE outperformed the WarpPINN model in this regard.

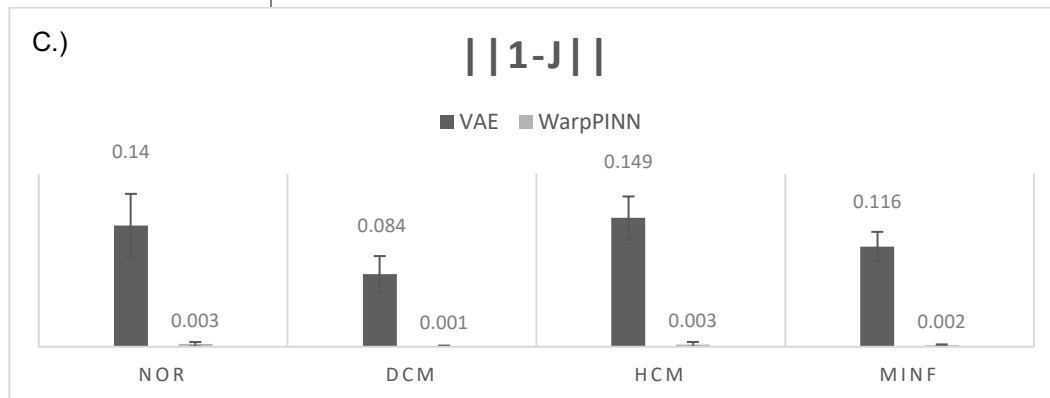
Conversely, the WarpPINN model showed a lower mean MCD value of 1.790 ± 1.553 mm than the VAE model's MCD mean value of 2.333 ± 0.573 mm with a p-value of 0.047. This result appears inconsistent as it implies that although the ground truth and the WarpPINN model's predicted myocardium segmentation overlap is lower, it more accurately estimated the boundary of the myocardium. Notably, this is not true for all pathology subsets. The mean MCD value of the VAE model was lower in the DCM (1.660 ± 0.221 mm) and MINF (1.549 ± 0.196 mm) model than the corresponding values of the WarpPINN model (DCM: 1.458 ± 1.829 mm; MINF: 1.789 ± 1.494 mm) as illustrated below in part B of Figure 3.3. In addition, in part C of Figure 3.3, we can discern that the WarpPINN model constrains deformation to a considerably lower degree of incompressibility compared to the VAE model with a mean difference of the determinant of the Jacobian of 0.122 ± 0.004 .



MODEL	Normal	DCM	HCM	MINF	Total
VAE - Mean(SD)	0.704(0.442)	0.832(0.021)	0.764(0.047)	0.801(0.038)	0.775(0.046)
WarpPINN – Mean(SD)	0.442(0.090)	0.624(0.092)	0.594(0.045)	0.525(0.150)	0.546(0.094)



MODEL	Normal	DCM	HCM	MINF	Total
VAE - Mean(SD)	3.123(0.939)	1.260(0.221)	3.398(0.934)	1.549(0.196)	2.333(0.573)
WarpPINN – Mean(SD)	2.429(1.653)	1.458(1.829)	1.484(1.237)	1.789(1.494)	1.790(1.553)



MODEL	Normal	DCM	HCM	MINF	Total
VAE - Mean(SD)	0.140(0.037)	0.084(0.021)	0.149(0.025)	0.116(0.017)	0.122(0.025)
WarpPINN – Mean(SD)	0.003(0.003)	0.001(0.001)	0.003(0.003)	0.002(0.001)	0.002(0.002)

Figure 3.3: Comparative Analysis between WarpPINN($n=38$) and VAE Generative model($n=40$) utilizing metrics the following metrics Mean Dice(A), Mean Contour Distance(B), and Mean Jacobian Determinant(C) across chosen disease states: Normal($n = 10$; $n=10$), Dilated Cardiomyopathy($n=8$; $n = 10$), Hypertrophic Cardiomyopathy($n=10$; $n=10$), and Myocardial Infarction with Altered LVEF($n=10$; $n=10$).

Discussion

4.1: Comparative Analysis of Biomechanical Models

In this study, we introduced a novel dataset to a recently developed method of image registration utilizing a physics-informed neural network. When presented with cine-MRI images of diverse myocardial pathologies including dilated cardiomyopathy, hypertrophic cardiomyopathy, and myocardial infarction, the WarpPINN model consistently achieved high SSIM values with low rates of error, giving new evidence of its robust performance and generalizability to compute myocardial strain for cardiomyopathies.

However, in comparison to the VAE model, WarpPINN overall showed a decreased Dice score and comparable but slightly improved MCD values indicating overall lower structural accuracy of WarpPINN's prediction of the myocardium. However, as the subset of images tested during the independent and comparative study are identical, the reason for the inconsistency between the low Dice score and favorable image-based metrics(SSIM and MSE) is unclear. It may indicate a possible error in the construction of the segmentation prediction when applying the deformation field to the reference segmentation. Current efforts are focused on identifying this error and improving this method.

Nevertheless, the VAE model's superior segmentation scores may also be attributed to working with less complex imaging as it was solely tested on 2D images while the WarpPINN model was tested to predict 3D deformations. In addition, the different methodologies of incorporating biomechanics between the two models may also partially account for the disparity in their segmentation scores. With the VAE's biomechanics prior and latent space representation, the

VAE model may have greater capacity for capturing essential features and noise reduction leading to more accurate predictions[26]. In addition, the weights of the parameters of the PINN model may have to be optimized in order to improve prediction scores. For example, the lower structural accuracy of the WarpPINN model could be a consequence of the greater weight placed on the incompressibility of the myocardium in WarpPINN, almost to a point of total incompressibility. Therefore, the LV deformation is highly restrained and the model's ability to predict the deformation of the myocardium may be dampened.

4.2: Limitations

Model Assumptions

The WarpPINN model makes several assumptions regarding the characteristics of the myocardium. It assumes that entirety of the myocardium is homogeneous, but the myocardial fibers change in orientation in the subepicardial, middle, and subendocardial layers. This changes how the myocardium contracts in different regions. In addition, factors such as scar tissue can also modify myocardial contraction. Furthermore, this model relies on passive contraction of the myocardium, but neglects active contraction of the cardiac myocytes which will affect strain estimation [27]. Also, the model inputs individual sets of patient images and forms predictions based off each set. However, the biomechanics are not personalised based off the pathology and structure of the myocardium of that patient. Therefore, the predictions may not be accurate in every patient. In addition to these assumptions, WarpPINN may not be practical clinically as it takes two to three hours for mesh generation and training before a prediction can be made and therefore may not be clinically efficient. Finally, with the current dice scores, its accuracy cannot be verified and therefore cannot be applied to clinical practice.

Mesh Generation

In two subjects with dilated cardiomyopathy, we were unable to generate a tetrahedral mesh using the TetGen package. Likely the thin myocardium in these subjects contain small regions that result in tetrahedra with high aspect ratios (ratio of the longest edge length to the shortest edge length) which can lead to a poor mesh quality and numerical instability. Therefore, the mesh generation may have been limited due to aspect ratio limits, poor quality elements, small feature sizes, or poorly defined geometry. In addition, as generating high quality meshes is computationally expensive, we forewent mesh smoothing and did not allow bisection which will create a less refined grid. However, this may have led to sacrificing the mesh's accuracy in modeling myocardial deformation as the mechanical behaviors of the cardiac tissue may deviate from reality leading to errors in registration and lower dice scores.

Discrepancy in Myocardial Incompressibility:

For decades now, the compressibility of the myocardium has been a subject of debate. In 1980, Tsukiji and Ritma published their findings demonstrating the preservation of the canine ventricular myocardial volume through systole and diastole utilizing video ventriculography [28]. Since then, multiple studies have used the near-incompressibility of the myocardium to inform the biomechanics of their respective models.

However, it should be noted that a 2020 study by Kumar et al. has demonstrated that healthy myocardium showed greater compressibility or volume change of almost 20% between the diastolic and systolic phase, compared to patient with dilated cardiomyopathy in which the myocardium showed minimal change in volume [29]. As mentioned above, our dataset contains both healthy and various pathological cardiac imaging. As the WarpPINN model also makes the same assumption of near incompressibility of the cardiac tissue for each input image data, the

disparity in compressibility in different pathologies could adversely affect the validity of the strain calculations.

4.3: Future Studies

In the immediate future, we are looking to enhance the accuracy of WarpPINN by improving mesh generation. Enhancing the quality of input meshes by incorporating smoothing functions may lead to a more refined model that better represents the myocardial deformation. In addition, we are conducting experiments to ascertain how the weight of incompressibility may change the accuracy of WarpPINN's image registration. Optimizing incompressibility based on pathology and analyzing the disparities could further inform biomechanical PINN models so they can be more personalised towards specific patient pathologies.

In the long term, we will look towards improving upon the WarpPINN methodology by incorporating a different type of neural network. Most imaging registration models employ convolutional neural networks(CNN) as opposed to fully connected neural networks such as WarpPINN as CNNs are more parameter-efficient, can learn hierarchical representations of visual features, and better preserve spatial information as a result of weight sharing through convolutional layers. A recent advancement in deep-learning is the emergence of physics-informed convolutional neural networks(PICNN). Such models have been applied to clinical tasks such as blood pressure estimation yielding favorable results with minimal training data [30]. As CNNs are ideal for image-based tasks, a viable route of future study would be to modify a PINN model such as WarpPINN by replacing the FCNN with a CNN for more efficient and accurate image processing and consequently, improved myocardial strain estimation.

Conclusion

The WarpPINN model showed robust structural similarity when predicting the reference image and low error rates in image registration when trained on a novel dataset with multiple cardiac pathologies indicating for the first time its versatility in computing cardiac strain for various forms of cardiomyopathies. However, in comparison to a VAE generative model, WarpPINN did not show the same structural accuracy, thereby refuting our initial hypothesis that its performance would be comparable to the VAE model.

References

1. Roth, G. A., Mensah, G. A., Johnson, C. O., Addolorato, G., Ammirati, E., Baddour, L. M., Barengo, N. C., Beaton, A. Z., Benjamin, E. J., Benziger, C. P., Bonny, A., Brauer, M., Brodmann, M., Cahill, T. J., Carapetis, J., Catapano, A. L., Chugh, S. S., Cooper, L. T., Coresh, J., Criqui, M., ... GBD-NHLBI-JACC Global Burden of Cardiovascular Diseases Writing Group (2020). Global Burden of Cardiovascular Diseases and Risk Factors, 1990-2019: Update From the GBD 2019 Study. *Journal of the American College of Cardiology*, 76(25), 2982–3021. <https://doi.org/10.1016/j.jacc.2020.11.010>
2. Blinderman, C. D., Homel, P., Billings, J. A., Portenoy, R. K., & Tennstedt, S. L. (2008). Symptom distress and quality of life in patients with advanced congestive heart failure. *Journal of pain and symptom management*, 35(6), 594–603. <https://doi.org/10.1016/j.jpainsymman.2007.06.007>
3. Murphy SP, Ibrahim NE, Januzzi JL. Heart Failure With Reduced Ejection Fraction: A Review. *JAMA*. 2020;324(5):488–504. doi:10.1001/jama.2020.10262
4. Brady, B., King, G., Murphy, R. T., & Walsh, D. (2023). Myocardial strain: a clinical review. *Irish journal of medical science*, 192(4), 1649–1656. <https://doi.org/10.1007/s11845-022-03210-8>
5. Rajiah, P. S., Kalisz, K., Broncano, J., Goerne, H., Collins, J. D., François, C. J., Ibrahim, E. S., & Agarwal, P. P. (2022). Myocardial Strain Evaluation with Cardiovascular MRI: Physics, Principles, and Clinical Applications. *Radiographics : a review publication of the Radiological Society of North America, Inc*, 42(4), 968–990. <https://doi.org/10.1148/rq.210174>
6. Scatteia, A., Baritussio, A., & Bucciarelli-Ducci, C. (2017). Strain imaging using cardiac magnetic resonance. *Heart failure reviews*, 22(4), 465–476. <https://doi.org/10.1007/s10741-017-9621-8>
7. Smiseth, O. A., Torp, H., Opdahl, A., Haugaa, K. H., & Urheim, S. (2016). Myocardial strain imaging: how useful is it in clinical decision making?. *European heart journal*, 37(15), 1196–1207. <https://doi.org/10.1093/eurheartj/ehv529>
8. Zhang, Y., Mui, D., Chirinos, J. A., Zamani, P., Ferrari, V. A., Chen, Y., & Han, Y. (2021). Comparing cardiovascular magnetic resonance strain software packages by their abilities to discriminate outcomes in patients with heart failure with preserved ejection fraction. *Journal of cardiovascular magnetic resonance : official journal of the Society for Cardiovascular Magnetic Resonance*, 23(1), 55. <https://doi.org/10.1186/s12968-021-00747-y>
9. West, A. M., & Kramer, C. M. (2009). Comprehensive cardiac magnetic resonance imaging. *The Journal of invasive cardiology*, 21(7), 339–345.
10. Raissi, M., Perdikaris, P., & Karniadakis, G.E. (2019). Physics-informed neural networks: A deep learning framework for solving forward and inverse problems involving nonlinear partial differential equations. *J. Comput. Phys.*, 378, 686–707.
11. López, P. A., Mella, H., Uribe, S., Hurtado, D. E., & Costabal, F. S. (2022). WarpPINN: Cine-MR image registration with physics-informed neural networks. *ArXiv. /abs/2211.12549*
12. Dwivedi, K. K., Lakhani, P., Kumar, S., & Kumar, N. (2022). A hyperelastic model to capture the mechanical behaviour and histological aspects of the soft tissues. *Journal of the mechanical behavior of biomedical materials*, 126, 105013. <https://doi.org/10.1016/j.jmbbm.2021.105013>
13. Boveiri, H. R., Khayami, R., Javidan, R., Mehdizadeh, A. (2020). Medical image registration using deep neural networks: A comprehensive review. *Computers & Electrical Engineering*, 87, 106767. ISSN 0045-7906. <https://doi.org/10.1016/j.compeleceng.2020.106767>.

14. Perumal L. (2019). New approaches for Delaunay triangulation and optimisation. *Heliyon*, 5(8), e02319. <https://doi.org/10.1016/j.heliyon.2019.e02319>
15. Rueckert, D., Aljabar, P., Heckemann, R. A., Hajnal, J. V., & Hammers, A. (2006). Diffeomorphic registration using B-splines. *Medical image computing and computer-assisted intervention : MICCAI ... International Conference on Medical Image Computing and Computer-Assisted Intervention*, 9(Pt 2), 702–709. https://doi.org/10.1007/11866763_86
16. De Craene, M., Piella, G., Camara, O., Duchateau, N., Silva, E., Doltra, A., D'hooge, J., Brugada, J., Sitges, M., & Frangi, A. F. (2012). Temporal diffeomorphic free-form deformation: application to motion and strain estimation from 3D echocardiography. *Medical image analysis*, 16(2), 427–450. <https://doi.org/10.1016/j.media.2011.10.006>
17. Vercauteren, T., Pennec, X., Perchant, A., & Ayache, N. (2008). Symmetric log-domain diffeomorphic Registration: a demons-based approach. *Medical image computing and computer-assisted intervention : MICCAI ... International Conference on Medical Image Computing and Computer-Assisted Intervention*, 11(Pt 1), 754–761. https://doi.org/10.1007/978-3-540-85988-8_90
18. Mansi, T., Pennec, X., Sermesant, M. et al. iLogDemons: A Demons-Based Registration Algorithm for Tracking Incompressible Elastic Biological Tissues. *Int J Comput Vis* **92**, 92–111 (2011). <https://doi.org/10.1007/s11263-010-0405-z>
19. Morales, M. A., Izquierdo-Garcia, D., Aganj, I., Kalpathy-Cramer, J., Rosen, B. R., & Catana, C. (2019). Implementation and Validation of a Three-dimensional Cardiac Motion Estimation Network. *Radiology. Artificial intelligence*, 1(4), e180080. <https://doi.org/10.1148/ryai.2019180080>
20. Qin, C., Wang, S., Chen, C., Bai, W., & Rueckert, D. (2023). Generative myocardial motion tracking via latent space exploration with biomechanics-informed prior. *Medical image analysis*, 83, 102682. <https://doi.org/10.1016/j.media.2022.102682>
21. Bernard, O., Lalande, A., Zotti, C., Cervenansky, F., Yang, X., Heng, P. A., Cetin, I., Lekadir, K., Camara, O., Gonzalez Ballester, M. A., Sanroma, G., Napel, S., Petersen, S., Tziritas, G., Grinias, E., Khened, M., Kollerathu, V. A., Krishnamurthi, G., Rohe, M. M., Pennec, X., ... Jodoin, P. M. (2018). Deep Learning Techniques for Automatic MRI Cardiac Multi-Structures Segmentation and Diagnosis: Is the Problem Solved?. *IEEE transactions on medical imaging*, 37(11), 2514–2525. <https://doi.org/10.1109/TMI.2018.2837502>
22. Si, H. (2015). TetGen, a Delaunay-Based Quality Tetrahedral Mesh Generator. *TOMS*, 41 (2).
23. Wan, M., Lim, C., Zhang, J., Su, Y., Yeo, S. Y., Wang, D., Tan, R. S., & Zhong, L. (2013). Reconstructing patient-specific cardiac models from contours via Delaunay triangulation and graph-cuts. *Annual International Conference of the IEEE Engineering in Medicine and Biology Society. IEEE Engineering in Medicine and Biology Society. Annual International Conference*, 2013, 2976–2979. <https://doi.org/10.1109/EMBC.2013.6610165>
24. H. L. Tan, Z. Li, Y. H. Tan, S. Rahardja and C. Yeo, "A Perceptually Relevant MSE-Based Image Quality Metric," in *IEEE Transactions on Image Processing*, vol. 22, no. 11, pp. 4447–4459, Nov. 2013, doi: 10.1109/TIP.2013.2273671.
25. Zou, K. H., Warfield, S. K., Bharatha, A., Tempany, C. M., Kaus, M. R., Haker, S. J., Wells, W. M., 3rd, Jolesz, F. A., & Kikinis, R. (2004). Statistical validation of image segmentation quality based on a spatial overlap index. *Academic radiology*, 11(2), 178–189. [https://doi.org/10.1016/s1076-6332\(03\)00671-8](https://doi.org/10.1016/s1076-6332(03)00671-8)
26. Zhong, W., & Meidani, H. (2022). PI-VAE: Physics-Informed Variational Auto-Encoder for stochastic differential equations. *ArXiv, abs/2203.11363*.
27. Fernandez-Teran, M. A., & Hurle, J. M. (1982). Myocardial fiber architecture of the human heart ventricles. *The Anatomical record*, 204(2), 137–147. <https://doi.org/10.1002/ar.1092040207>
28. Tsuike, K., & Ritman, E. L. (1980). Direct evidence that left ventricular myocardium is incompressible throughout systole and diastole. *The Tohoku journal of experimental medicine*, 132(1), 119–120. <https://doi.org/10.1620/tjem.132.119>
29. Kumar, V., Ryu, A. J., Manduca, A., Rao, C., Gibbons, R. J., Gersh, B. J., Chandrasekaran, K., Asirvatham, S. J., Araoz, P. A., Oh, J. K., Egbe, A. C., Behfar, A., Borlaug, B. A., & Anavekar, N. S. (2021). Cardiac MRI demonstrates compressibility in healthy myocardium but not in myocardium with reduced ejection fraction. *International Journal of Cardiology*, 322, 278–283. <https://doi.org/10.1016/j.ijcard.2020.08.087>
30. Sel, K., Mohammadi, A., Pettigrew, R.I. et al. Physics-informed neural networks for modeling physiological time series for cuffless blood pressure estimation. *npj Digit. Med.* **6**, 110 (2023). <https://doi.org/10.1038/s41746-023-00853-4>

Appendix A: Abbreviations(Alphabetized)

Abbreviation	Expansion
ACDC	Automatic Cardiac Diagnosis Challenge
ARV	Abnormal Right Ventricular Function
BINN	Biomechanics-Informed Neural Network
CNN	Convolutional Neural Network
DCM	Dilated Cardiomyopathy
FCNN	Fully Connected Neural Network
FFD	Free-Form Deformations
HCM	Hypertrophic Cardiomyopathy
HF	Heart Failure
HFmEF	Heart Failure with Minimally Reduced Ejection Fraction
HFpEF	Heart Failure with Preserved Ejection Fraction
HFrEF	Heart Failure with Reduced Ejection Fraction
LVEF	Left Ventricular Ejection Fraction
MINF	Myocardial Infarction with Altered Left Ventricular Ejection Fraction
MRI	Magnetic Resonance Imaging
MSE	Mean Square Error
NOR	Normal Cardiac Function
CMRI	Cine-Magnetic Resonance Imaging
PDE	Partial Differential Equation
PICNN	Physics-Informed Convolutional Neural Network
PINN	Physics-Informed Neural Network
SSFP	Steady-State Free Precession
SSIM	Structural Similarity Index Measure
TDFFD	Temporal Diffeomorphic Free Form Deformation
VAE	Variational Autoencoder

Appendix B: Pathology Descriptions Included in ACDC Dataset[21]

- **NOR:** Normal cardiac function with ejection fraction greater than 50% and the diastolic wall less than 12 mm. LV diastolic volume is less than 90 mL/m² for males and 80 mL/m² for females. The RV is normal for each patient (RV volume less than 100 mL/m² and RV ejection fraction above 40%). The visual analysis of the segmental LV and RV myocardial contraction is normal.
- **MINF:** Myocardial infarction with systolic heart failure with ejection fraction below 40% and abnormal myocardial contractions. Subset of patients may have high diastolic LV volume due to left ventricular compensatory remodeling post-infarction.
- **DCM:** Dilated cardiomyopathy with ejection fraction below 40% and an end-diastolic volume greater than 100 mL/m² and diastolic wall thickness less than 12 mm. Subset of DCM patients have a dilated right ventricle and/or a high left ventricular mass.
- **HCM:** Hypertrophic cardiomyopathy with ejection fraction greater than 55% but with left ventricular myocardium thicker than 15 mm in diastole. These patients can present with elevated cardiac mass indices above 110 g/m².
- **ARV:** Abnormal right ventricle with RV volume greater than 110 mL/m² in males and 100 mL/m² in females, and/or an RV ejection fraction less than 40%. Most subjects in this subgroup have a normal left ventricle.